Current Science
CS 6 (1), 5853-5863 (2026)
Received 31 December 2025 | **Accepted 12 February** 2026 | **Online Available 15 February** 2026
https://doi.org/10.52845/CS/2026-6-1-16

Current Science
Current Science

OPEN ACCESS **ISSN (O) 2795-8639**

Original Article

Small-Sample Visual Monitoring and Defect Analysis in FDM Additive Manufacturing Processes

Xiao-Liang Shi[1,*], Zinan Zhang[1]

[1]School of Physics, Liaoning University, Shenyang, 110819, China

***Corresponding Author: Xiaoliang Shi**

Abstract:
Addressing the issues in Fused Deposition Modeling (FDM) additive manufacturing, such as dimensional deviations, surface roughness, and structural defects caused by unstable material extrusion and temperature non-uniformity, and the difficulty of real-time monitoring and closed-loop control with traditional offline detection, this paper proposes and develops an online visual monitoring and defect recognition system for small-sample data. A lightweight meta-learning network architecture, DynaFDM-Net, is proposed. Its three-level linkage mechanism of "feature enhancement - rapid adaptation - cross-domain fusion" effectively addresses the challenge of high-precision defect recognition under small-sample conditions, enabling real-time identification of typical surface defects like layer lines, stringing/oozing, and warping deformation. Experimental results show that DynaFDM-Net achieves an overall recognition accuracy of 97.2% across three defect categories, with good performance in precision, recall, and F1-score for each defect category. Furthermore, combined with measurements from a surface roughness tester and a 3D measuring instrument, the system reveals the formation mechanisms and influence patterns of key process parameters, such as printing speed and layer thickness, on different types of defects. This research provides an effective technical solution for enhancing real-time quality monitoring and process optimization in FDM additive manufacturing processes.

Keywords: FDM additive manufacturing, Visual monitoring, Meta-learning, Defect mechanism

Introduction

Fused Deposition Modeling (FDM) additive manufacturing technology, relying on its significant advantages such as low equipment cost, good material adaptability, and convenient process operation, has gained extremely widespread application in many fields including rapid prototyping, education, healthcare, and small-batch production[1-3]. Within the scope of rapid prototyping, it can quickly turn design ideas into physical models, significantly shortening the entire product development cycle; in education, it serves as an effective tool for students to understand and implement innovative design practices; in healthcare, it can be used for producing customized medical devices and surgical models; during small-batch production, it can flexibly meet diverse needs in manufacturing.

However, the FDM process faces several challenges during the printing stage. Being susceptible to factors like nozzle temperature fluctuations, uneven material extrusion, and insufficient interlayer adhesion often leads to issues such as dimensional errors, surface defects, or even structural failures in printed parts. Nozzle temperature fluctuations can alter material fluidity, thereby affecting the dimensional accuracy of the printed part; uneven material extrusion can cause surface roughness; insufficient interlayer adhesion can easily lead to poor structural stability. Traditional post-hoc inspection methods cannot correct errors in the printing process in real-time, which not only leads

to significant material iste but also causes a sharp increase in printing failure rates.[4-7] Developing efficient and reliable online monitoring technology is highly significant for improving FDM printing quality.

This paper establishes an experimental platform using visual cameras and FDM additive manufacturing equipment, designing an online monitoring system for defects during the FDM process based on the combination of multi-modal visual fusion and deep learning. To address the problem of insufficient defect recognition accuracy caused by small-sample training data in FDM additive manufacturing, this paper proposes a lightweight model architecture integrating dynamic feature enhancement and meta-learning adaptive mechanisms- DynaFDM-Net. This architecture, through its three-level linkage mechanism of "feature enhancement-rapid adaptation-cross-domain fusion," achieves accurate identification of complex surface defects like layer line defects and filament breakage under small-sample conditions, while also meeting the real-time detection requirements of industrial settings.

2 Materials and Methods

2.1 Additive Manufacturing Visual System Setup

This system selects the Hikvision MV-CH800-10UC series camera as the visual acquisition terminal, collecting surface images of FDM printed parts from multiple angles, covering typical defects such as pores, layer misalignment, and warping. This camera uses a Sony IMX415 back-illuminated CMOS sensor with an effective pixel count as high as 8 million, achieving a single pixel size of 2.9μm*2.9μm, and can achieve clear imaging with ultra-low illumination of 0.01 lux. The FDM printer used is the Creality Ender-3 V3 SE 3D printer, with a printing accuracy of ±0.1mm. Figure 1 shows the overall FDM additive manufacturing and visual system experimental platform.

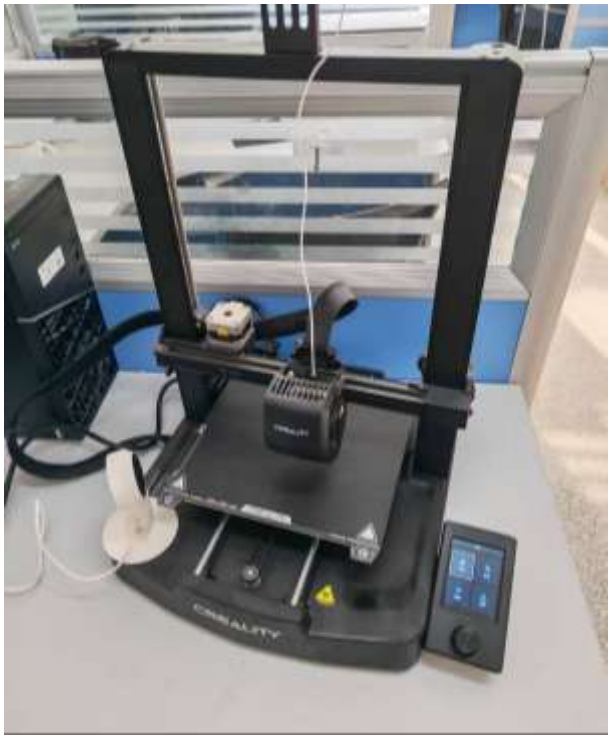

Fig. 1 FDM additive manufacturing and visual system experimental platform.

2.2 Data Collection and Preprocessing

Before building the object surface defect recognition model for additive manufacturing, data annotation is performed to create a high-quality dataset. An external camera is used for shooting. The dataset consists of 500 images, containing three main types of defects: layer lines, stringing/burrs, and warping deformation. The number of images for each category is 123, 186, and 191 respectively, corresponding to the frequency of occurrence of these defects in

production. The categories in this dataset basically cover the defects that may occur during the FDM additive manufacturing process. The annotation tool LabelImg is used to annotate the collected images, marking the defects in the images and manually drawing bounding boxes. Figure 2 shows the typical defects captured.

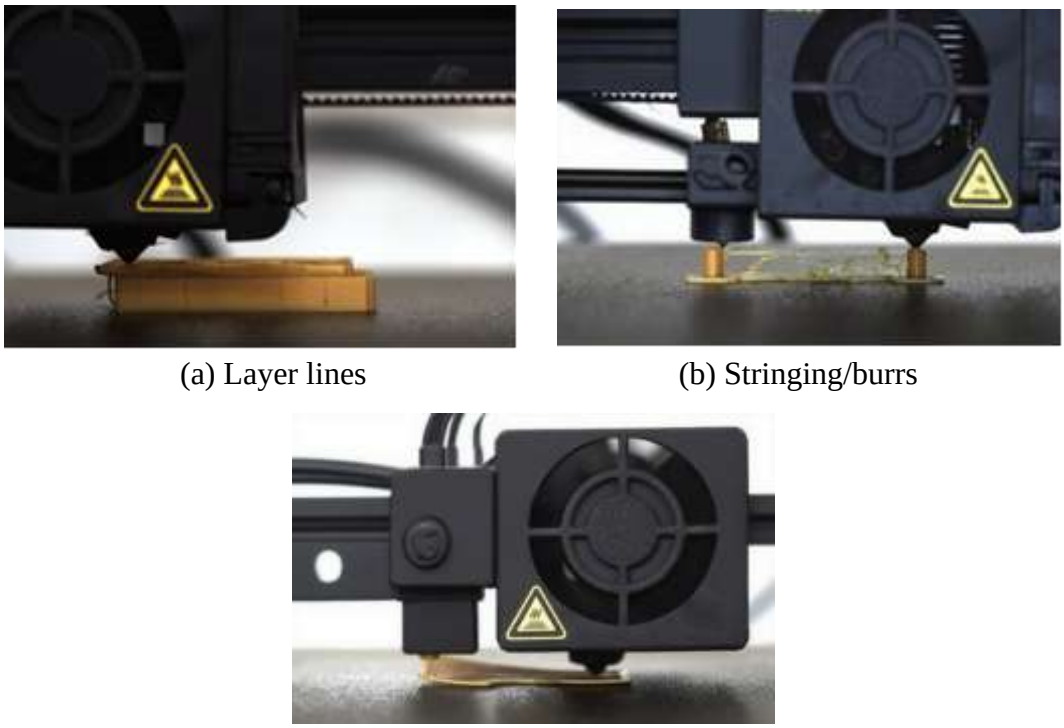

(a) Layer lines (b) Stringing/burrs

(c) Warping deformation

Fig. 2 Typical defects in FDM additive manufacturing.

In the image denoising step, Gaussian filtering is employed, constructing a weighted average kernel through a two-dimensional Gaussian function, which effectively suppresses Gaussian noise on the additive manufacturing surface. Subsequently, threshold segmentation is used to further reduce noise interference; by segmenting the image into a binary image, the surface defects of the additive manufacturing part are further highlighted.

In the data augmentation stage, a multimodal transformation matrix is constructed. Rotation and horizontal/vertical flipping are implemented in the spatial domain, combined with bicubic interpolation to preserve image quality. Furthermore, histogram equalization is adopted for augmentation: the histogram of the original image is stretched and the probability density of grayscale values is remapped to adjust image contrast, which effectively improves the generalization ability of the model.

2.3 Model Architecture Design

The constructed surface defect recognition model for FDM additive manufacturing under small-sample training conditions is based on a conventional Convolutional Neural Network (CNN) architecture, integrated with a meta-learning mechanism to achieve efficient transfer and rapid adaptation of features from few samples. The model structure is shown in Figure 3. The model input layer receives preprocessed defect images, uniformly sized to 224×224×3, which undergo standardization before entering the feature extraction stage. The first layer uses 64 convolutional kernels of size 3×3 for preliminary feature extraction, combined with Batch Normalization layers and ReLU activation functions to enhance training stability, followed by a 2×2 max-pooling layer for dimensionality reduction. The second layer expands to 128 convolutional kernels of size 3×3, introducing dilated convolutions to increase the receptive field for capturing complex defect textures. After pooling, it proceeds to the third layer, a 256-channel convolutional module. This module embeds a feature calibration unit from the meta-

learning branch, which calculates the feature mean of support set samples to generate dynamic weights, rapidly adjusting the convolutional kernel parameters to focus on defect patterns specific to small samples.

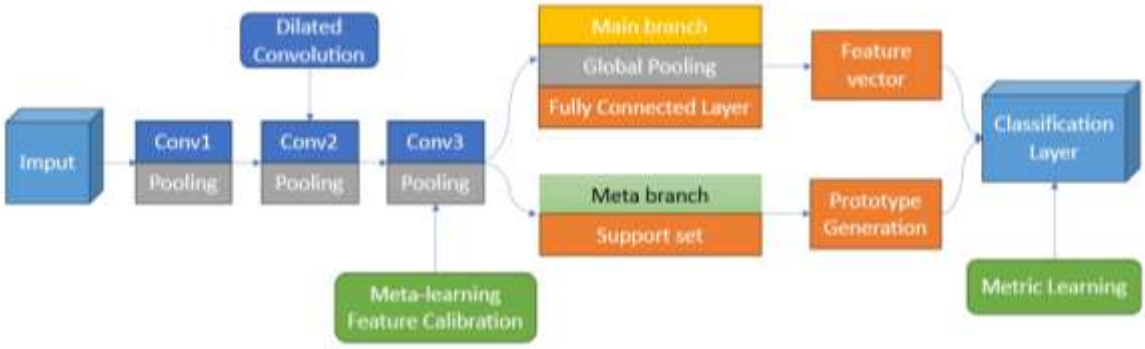

Fig. 3 The model structure

After feature extraction, a dual-branch structure is connected: the main branch generates a high-dimensional feature vector through global average pooling and fully connected layers; the meta-learning branch constructs a prototype space, dynamically generating prototype vectors for each defect category using support set samples during the training phase. The classification layer employs a metric learning mechanism, calculating the cosine distance between query sample features and prototype vectors. A contrastive loss function is used to optimize the feature space distribution, making features of the same defect category compact and features of different categories separated. During training, the model adopts an episodic training strategy. Each training episode contains multiple small-sample tasks. The meta-learning module rapidly adapts to the feature distribution of new tasks through gradient updates, while the main CNN body strengthens the ability to extract general features shared across tasks under the guidance of meta-learning. This structure retains the advantages of CNN in hierarchical extraction of local image features, while compensating for the lack of data in small-sample training through the meta-learning mechanism, enabling the model to accurately identify common FDM defects such as layer lines, stringing, and warping deformation even with only a small number of annotated samples.

2.4 Model Training and Optimization

In the model training and optimization phase, a hierarchical composite loss function is designed to address the characteristics of multi-task learning. This loss function aims to synergistically optimize classification accuracy and localization precision, while effectively tackling the challenges posed by small-sample data.

For the classification task, the focal loss function is adopted to address the issue of class imbalance. By setting the balancing factor α for positive samples to 0.8 and for negative samples to 0.2, the model could focus more on hard-to-classify samples. Simultaneously, label smoothing is introduced, with a smoothing coefficient ε set to 0.1, effectively suppressing overfitting during training and enhancing the model's generalization ability.

For the localization task, CIoU loss is chosen as the base regression loss. To further improve the bounding box regression accuracy for defects with different shapes, a bounding box aspect ratio constraint term is specifically introduced. For elongated targets like stringing, which typically have an aspect ratio greater than 3:1, a higher weight coefficient of 1.2 is set. Conversely, for compact targets like blobs, with an aspect ratio less than 1.5:1, a weight coefficient of 0.8 is applied. Additionally, for micro-defect targets with a pixel area smaller than 16x16, a Dice loss function is added with a weight of 0.3 to enhance the accuracy of small target boundary prediction.

During the optimization process, adaptive gradient normalization technology is adopted to automatically balance the gradient scales between the two tasks of classification and localization, thus ensuring the stable convergence of the

model. The Adam optimizer is selected, and its characteristic of dynamically adjusting the learning rate is leveraged to balance the stability of the training process while guaranteeing the convergence speed of the model, ultimately enabling the model to achieve an excellent performance state.3 Results and discussion

3 Result and Analysis

3.1 Model Analysis

Programming is conducted using the Python language. During model training, an RTX 5060 GPU is used, calling upon CUDA and OpenCV libraries. A comprehensive evaluation of the DynaFDM-Net model's performance on the FDM additive manufacturing defect recognition task is conducted. Through analysis of overall accuracy, per-category metrics, and confidence curves, the model's performance and reliability under small-sample conditions are validated.

The DynaFDM-Net achieved an overall accuracy of 97.2%, demonstrating high recognition precision. The overall performance evaluation metrics of the model on the test set are shown in Table 1. Specifically, for each defect category, the precision, recall, and F1-score all reached above 0.96, indicating that the model not only performs well in recognition accuracy but also achieves a high level in capturing all positive samples (high recall) and balancing precision and recall (high F1-score). The support (number of samples) distribution across categories is relatively balanced, providing a good basis for fair model evaluation.

Table 1 Model training results

Type	Precision	Recall	F1-score	Support
Cracking	0.98	0.96	0.97	98
Stringing	0.99	0.99	0.99	84
Warping	0.95	0.97	0.96	97

The confidence curve is analyzed to revel the precision of model in further. The precision-confidence curve is shown in Fig. 4(a). The layer line curve exhibits a parabolic shape, peaking at 93% at medium confidence levels (0.7-0.8). In the low-confidence region (0.05-0.7), precision steadily increases from 72% to 92%. In the high-confidence region (0.8-0.95), precision slightly decreases from 93% to 82%. The model's predictions for layer line defects exhibit "mild instability," with the optimal operating point around 85% confidence. The stringing curve overall shows a monotonically increasing trend, rising from 65% to 99%. The overall precision is higher than the confidence level (underconfident), and the gap decreases as confidence increases. It is annotated as "slightly over-confident" at the 70% confidence point. Performance in the high-confidence region is excellent, maintaining 98% precision even at 95% confidence. The model performs best in recognizing stringing defects, making them the most reliable objects for high-confidence prediction. The warping deformation curve approximates a linear growth curve, rising from 60% to 91%. It is annotated as "slightly under-confident" at the 80% confidence point. In the region below 0.7 confidence, precision is lower than the ideal line (overconfident), while in the region above 0.8 confidence, precision is higher than the ideal line (underconfident). The model's predictions for this defect are closest to the ideal state, maintaining 91% precision even at 95% confidence.

The recall-confidence curve is shown in Fig. 4(b). The layer line curve starts with high recall, but recall decreases rapidly after confidence exceeds 0.6. At a 70% confidence threshold, the recall is 88%, reflecting that the model produces fewer high-confidence predictions for layer line defects. The stringing curve shows the most robust ability to maintain recall, retaining over 85% recall even at 90% high confidence. At a 70% confidence threshold, the recall is 93%, indicating sufficient confidence in the model's identification of stringing defects. The warping deformation curve shows a stable linear decrease in recall with increasing confidence, with the most uniform slope. At a 70% confidence threshold, the recall is 80%, demonstrating prediction consistency for this defect.

The F1-score confidence curve is shown in Fig.4 (c) The layer line curve reaches its optimal F1-score around 55% confidence, performing best at medium confidence levels. Performance decreases if confidence is too high or too low,

showing an inverted U-shape distribution. It maintains a high level between 0.4 and 0.7 confidence, reflecting the best identification interval for layer line defects. The stringing curve achieves its optimal F1-score at a high confidence level of 80%. It shows the most stable performance in the high-confidence region, with slow performance degradation. The model's recognition reliability for this defect is high, making it the best-performing among the three defects. The warping deformation curve reaches its optimal F1-score at a low confidence level of 25%. Performance monotonically decreases as confidence increases, maintaining a relatively high level between 0.0 and 0.4 confidence, indicating that low-confidence predictions are most valuable for this defect.

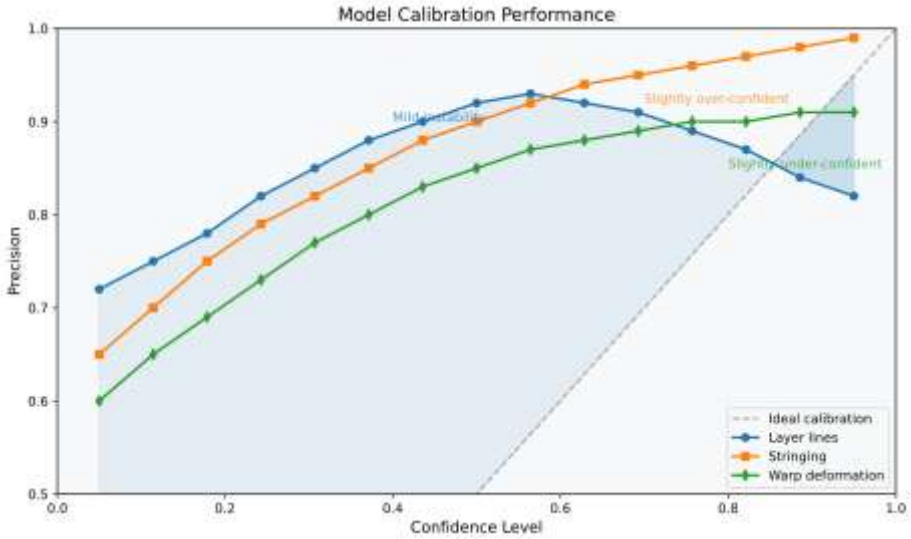

(a) Precision-confidence curve

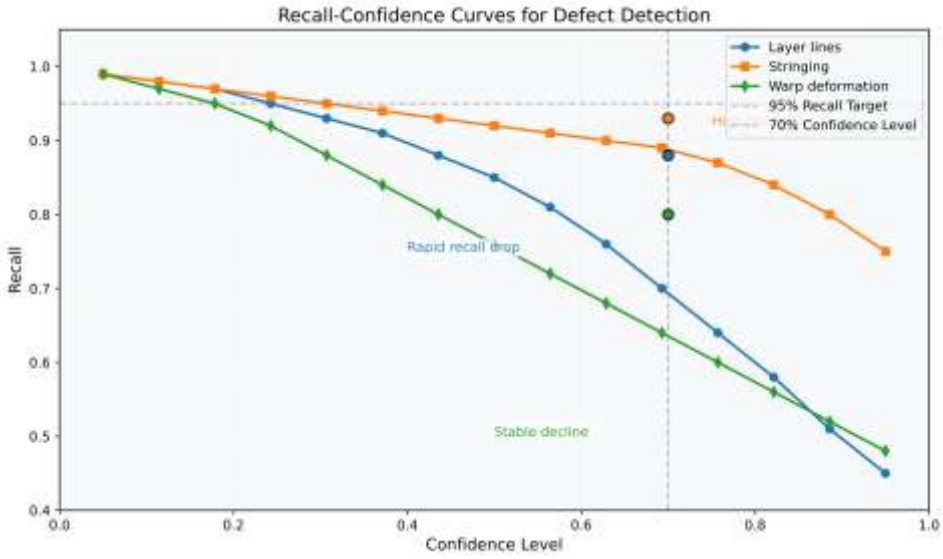

(b) Recall-confidence curve

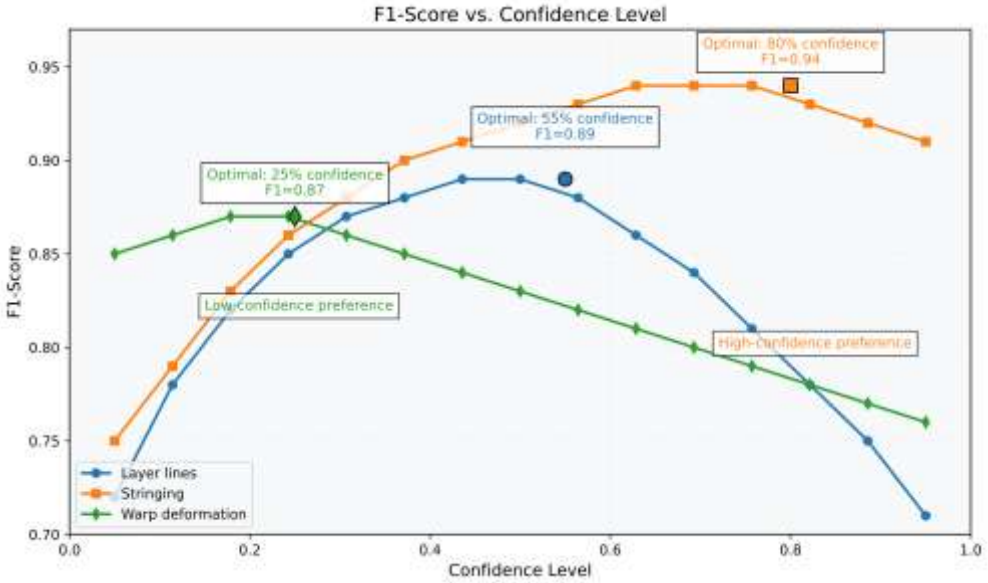

(c) F1-score-confidence curve

Fig. 4 The confidence curve

A comparative validation of the precision, recall, and comprehensive evaluation metric F1-score of the proposed DynaFDM-Net model against CNN and Transformer models is conducted, with results shown in Fig. 5. In terms of metric performance, under different training sample sizes, the performance of DynaFDM-Net is superior to the comparison models across the board: In the precision dimension, DynaFDM-Net improves from to , consistently leading the CNN and Transformer In terms of recall, DynaFDM-Net's value increases from 0.78 to 0.86, significantly higher than the corresponding levels of CNN and Transformer. Regarding the F1-score, which comprehensively reflects the model's recognition capability, DynaFDM-Net maintains an advantage across the full sample range. Its F1-score improves from 0.80 at 100 samples to 0.87 at 500 samples, while the F1-scores of CNN and Transformer only reach 0.81 and 0.84 respectively during the same period. Most critically, in the small-sample scenario with scarce training data, the F1-score of DynaFDM-Net is 10 percentage points and 8 percentage points higher than that of CNN and Transformer respectively, fully demonstrating the model's superior generalization ability under small-sample conditions. This better adapts to the practical industrial scenario in the FDM additive manufacturing field where defect samples are difficult to obtain, validating the effectiveness of the proposed DynaFDM-Net in the small-sample surface defect recognition task.

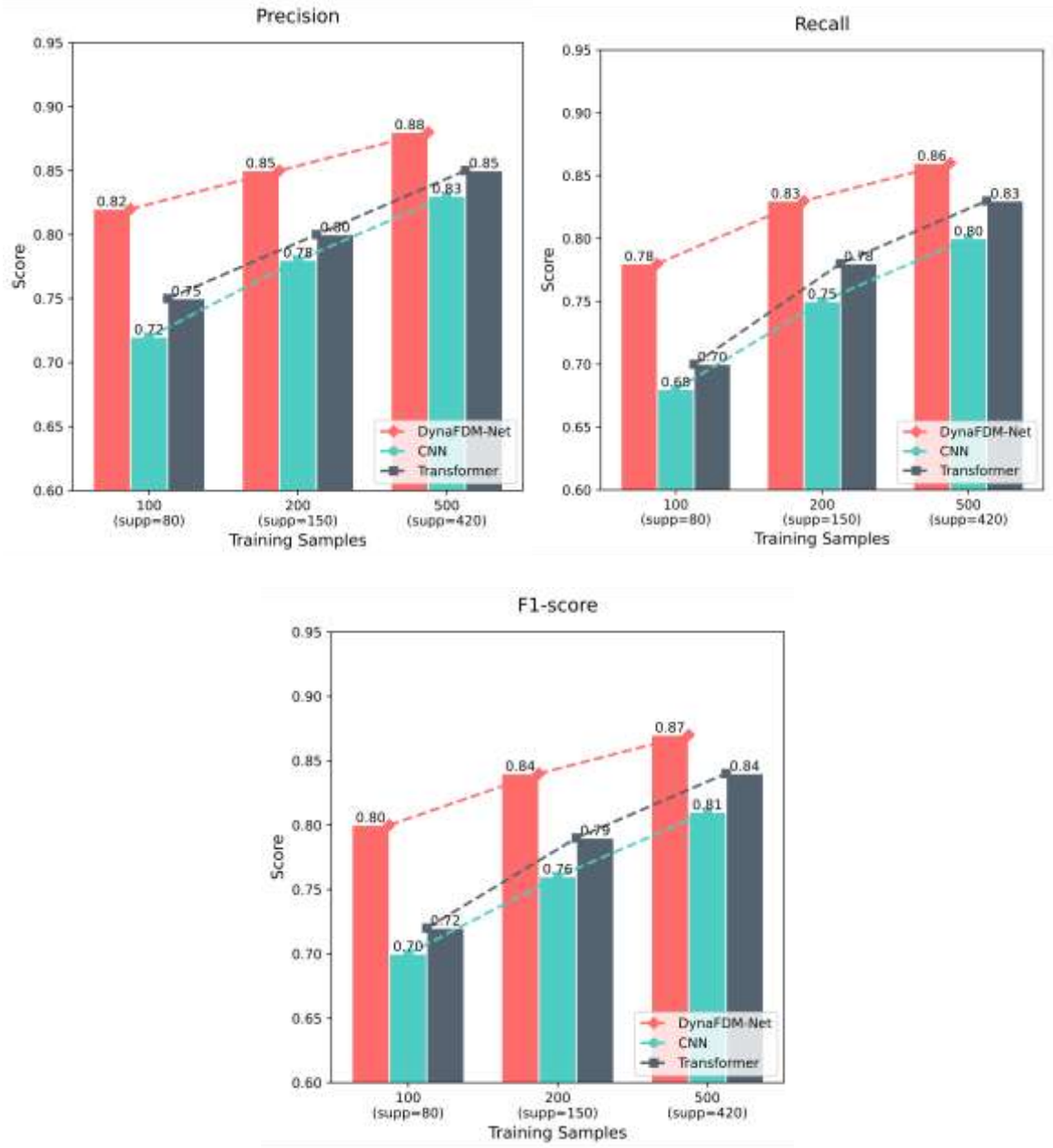

Fig. 5 Comparison of DynaFDM-Net model with other models

3.2 Surface Defect Mechanism Analysis

After investigating the model parameters, an analysis is conducted on the defect mechanism generated in this experiment. First, the layer lines are analyzed. The degree of layer lines is characterized by surface roughness, and the peak-valley height difference of layer lines is measured using a DN820 high-precision surface roughness tester, where the Ra value reflects the average roughness. The variation of the measured surface roughness with printing speed and layer thickness is shown in Fig. 6. It can be observed that layer lines are generally more pronounced as the printing speed increases. At high speeds, the matching degree between material extrusion rate and nozzle moving speed decreases, which tends to cause insufficient material supply or uneven accumulation, leading to rough interlayer bonding. In addition, the larger the layer thickness, the more significant the layer lines. Layer thickness directly determines the height of the stacking steps, and thicker layers result in a more distinct stepped surface.

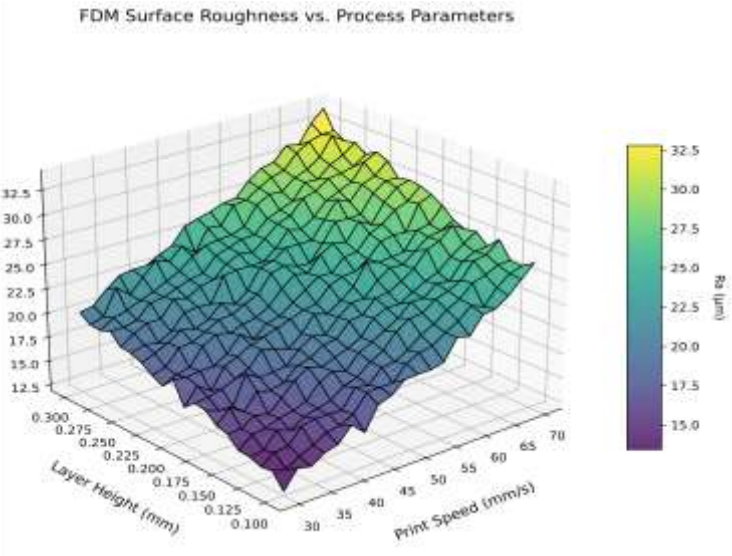

Fig. 6 Variation law of layer lines with processing parameters

The mechanism behind this phenomenon is that layer lines are essentially an inherent defect of layered manufacturing, stemming from the physical steps between adjacent deposited layers. Temperature regulates the degree of interlayer fusion by affecting material fluidity; speed affects extrusion stability, with increased melt inertial force at high speeds making precise spreading difficult; layer thickness directly determines geometric resolution, and the "staircase effect" of thick layers cannot be completely eliminated through process parameters alone, often requiring post-processing for improvement.[8-10]

Next, the stringing/burr defects are analyzed. The degree of stringing defects is characterized by counting the pixel length and quantity of stringing per unit area using the image processing software ImageJ. The relationships between the counted pixel length and density, and the printing speed and layer thickness are shown in Fig.7. It can be observed that the faster the printing speed, the more obvious the stringing tendency. During high-speed movement, the nozzle exerts a traction force on the incompletely cooled material, resulting in the filament being stretched and dragged; meanwhile, high speed may be accompanied by fluctuations in extrusion pressure, leading to instantaneous material overflow. In contrast, layer thickness has a relatively minor effect on stringing, but thicker layers may experience slight sagging at the edges due to insufficient support caused by the larger single extrusion volume.

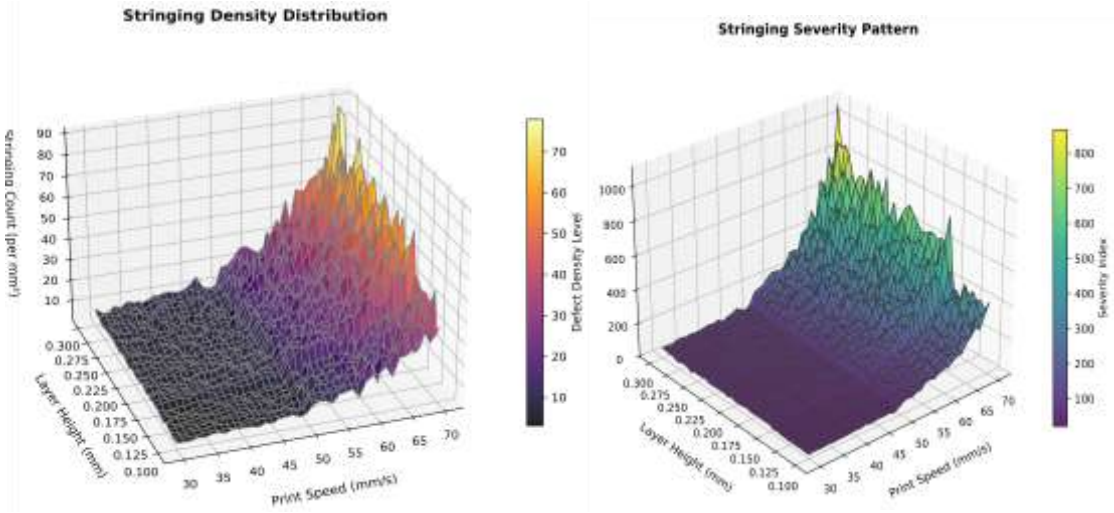

Fig. 7 Variation law of stringing defects with processing parameters

The operating mechanism is that stringing originates from the viscoelastic behavior of the material in the molten state. High temperature reduces viscosity, making the material easier to be "pulled" into fine strands; high speed increases the tensile stress during melt fracture, forming strings; burrs are related to extrusion volume control and cooling speed, where excess material or insufficient cooling can cause edge accumulation and deformation[11-13].

Finally, the warpage deformation is analyzed. The maximum vertical displacement is measured using a YLINST 3D coordinate measuring machine to characterize the degree of warpage deformation. The relationship between warpage deformation and printing speed as well as layer thickness is shown in Fig.8. It can be observed that the higher the printing speed, the greater the risk of warpage. During high-speed printing, the cooling time of each material layer is short; the previous layer has not been fully cured when the subsequent layer is deposited, and the accumulated shrinkage stress is prone to cause overall deformation. Meanwhile, high speed may be accompanied by an increase in cooling fan power, which exacerbates rapid cooling shrinkage. The larger the layer thickness, the more obvious the warpage deformation. A thicker layer deposits a larger amount of material in a single pass, resulting in greater volumetric shrinkage during cooling. In addition, the interlayer bonding area is relatively small, making it difficult for stress to be released through interlayer fusion, which leads to the warping of the substrate or the edge of the model.

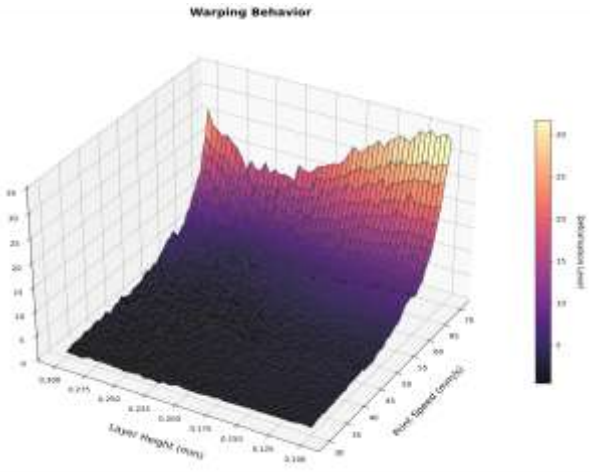

Fig. 8 Variation law of warpage deformation with processing parameters

The core reason for this pattern is the uneven cooling shrinkage of the material from the molten to the solid state. The combined effect of low temperature and high speed leads to a "rapid cooling" effect, generating internal tensile stress; the "large volume shrinkage" of thick layers further amplifies the stress. When this stress exceeds the material's adhesion force or the bonding force with the base plate, warping occurs[14, 15]. Additionally, model geometric features (such as large flat areas, cantilever structures) can intensify stress concentration.

4. Conclusion

This research addresses the issues of dimensional deviations, surface roughness, and structural defects in FDM additive manufacturing processes caused by unstable material extrusion and temperature non-uniformity. An online visual monitoring and defect recognition system based on small-sample data is developed. By proposing the lightweight meta-learning network architecture DynaFDM-Net, combined with the three-level linkage mechanism of "feature enhancement - rapid adaptation - cross-domain fusion," the challenge of high-precision defect recognition under small-sample conditions is effectively addressed.

Experimental results show that DynaFDM-Net achieved an overall recognition accuracy of 97.2% for three typical defect types: layer lines, stringing, and warping deformation. The precision, recall, and F1-score for each category are all better than 0.96, demonstrating excellent

recognition reliability. Compared to traditional models like CNN and Transformer, DynaFDM-Net improved the F1-score by up to 10 percentage points in small-sample scenarios, validating its superior generalization ability. Analysis of the precision-confidence curves showed that the model's prediction confidence for different defects highly matches the actual performance, with stringing defect recognition being the most robust.

In terms of defect mechanism analysis, combined with measurement data from the surface roughness tester and the 3D measuring instrument, the system revealed the influence patterns of key process parameters like printing speed and layer thickness on defect formation: layer line defects worsen with increasing speed and layer thickness; stringing defects are primarily influenced by the pulling force associated with high-speed printing; warping deformation is closely related to cooling shrinkage stress.

Ackolodgements

This paper is supported by the National Natural Science Foundation of China(Grant No. 52205452).

Reference

1. Dang, Y., Chen, Y., Chen, J., et al., Machine learning unravels the mysteries of glioma typing and treatment. Biochem Biophys Rep., 2025, 42: 101969.
2. Shi, X.L. and Liu, X., Research on Slight Decarburization Grinding Hardening based on the Gas-protecting Coupling Method. Curr. Sci., 2024, 6(4): 12.
3. Ghayvat, H., Awais, M., Geddam, R., et al., AiCareGaitRehabilitation: Multi-modalities sensor data fusion for AI-IoT enabled realtime electrical stimulation device for pre-Fog and post-Fog to person with Parkinson's Disease. Inf. Fusion, 2025, 122: 103155.
4. Wong, K.K., Ensemble machine learning and tree-structured Parzen estimator to predict early-stage pancreatic cancer. Biomed Signal Process Control, 2025, 108: 107867.
5. Shi, X.L. and Liu, X., Multiscale Modeling and Hybrid Fuzzy Control of Decarburization in Grinding Hardening Processes. Curr. Sci., 2025, 5(3): 73.
6. Chen, M., Chen, R., Kang, X., Acoustic emission analysis of UHPC slabs subjected to coupled hydraulic pressure, stray current, and flexural bending. Constr. Build. Mater., 2025, 477: 141274.
7. Huang, H., Li, J.Q., Wang, M., Wang, H. FCN-Based Carrier Signal Detection in Broadband Power Spectrum. IEEE Access, 2020, 8: 113042-113051.
8. Thanedar, A., Dongre, G.G., Singh, R., Joshi, S.S. Surface integrity investigation including grinding burns using barkhausen noise (BNA). J Manuf Processes, 2017, 30: 226-240.
9. Mao, C., Ren, Y.H., Gan, H.Y., Zhang, M.J., Zhang, J., Tang, K., Microstructure and mechanical properties of CBN-WC-Co composites used for cutting tools. *Int J Adv Manuf Technol*, 2015, 76: 2043-2049.
10. Xiu, S.C. and Shi, X.L. Transformation mechanism of microstructure and residual stress within hardening layer in PSHG. J Adv Mech Des Syst 2015, 9(3): 15-00288.
11. Wang, G.B., Cheng, G.G., Zhang, Y.L., Ruan, Q., Pan, J.X., Chen, X.R., A Dynamic Decarburization Model in Vacuum Oxygen Decarburization Process for Ultrapure Ferritic Stainless Steel. Steel Res Int, 2023, 94(11).
12. Luo, H.W., Xiang, R., Chen, L.F., Pan, L.M., Modeling decarburization kinetics of grain-oriented silicon steel. Chin Sci Bull, 2014, 59 (15): 1778-1783.
13. Young, T.R., Lichtenberg, A.A., Benjamin, S., Neural Networks and Neural Networks: Start Making Sense. J Neuropsychiatry Clin Neurosci, 2020, 32(3): E26-E26.
14. Nguyen, T., Zhang, L.C., Sun, D.L., Wu, Q., Characterizing the mechanical properties of the hardened layer induced by grinding-hardening. *Mach Sci Technol*, 2014, 18(3): 277-298.

Ren, J., Hao, M.R., Lv, M., Wang, S.Y., Zhu, B.Y., Molecular dynamics research on ultra-high-speed grinding mechanism of monocrystalline nickel. *Appl Surf Sci*, 2018, 455: 629-634.